

## Electromagnetically-induced focusing

Richard R. Moseley,\* Sara Shepherd, David J. Fulton, Bruce D. Sinclair, and Malcolm H. Dunn  
*J. F. Allen Physics Research Laboratories, Department of Physics and Astronomy, University of St. Andrews  
 St. Andrews, Fife KY16 9SS, Scotland*

(Received 20 June 1995; revised manuscript received 1 September 1995)

The theoretical basis for electromagnetically-induced focusing (EIF), which is caused by spatial variations in the coupling laser strength in an electromagnetically-induced transparency (EIT) experiment, is studied in detail. Using a numerical model it is shown that radial changes in both absorption and refractive index are important in predicting the probe beam's propagation conditions. Detailed calculations of the focusing and defocusing during EIF under various conditions are presented and compared with appropriate experiments. Diffractionlike patterns are predicted for, and observed on, a probe beam after propagation through a smaller EIT aperture.

PACS number(s): 42.50.Gy, 42.25.Bs, 42.50.Hz, 42.60.Jf

### I. INTRODUCTION

Recently it was demonstrated that within an electromagnetically-induced transparency (EIT) experiment [1,2] the Gaussian transverse intensity profile of the coupling laser beam led to focusing and defocusing observed on the weak probe laser beam [3]. This electromagnetically-induced focusing (EIF) was attributed to the spatially varying refractive index profile in the vapor cell caused by the range of coupling laser intensities at different transverse points within the beam. In this paper we present the results of detailed calculations for the propagation of the probe beam within such an experiment, including the change in both refractive index and absorption, and show that the focusing and defocusing induced on the probe laser are due to a combination of absorption and refractive index effects. This radically alters the expected variation in probe beam sizes after the EIT region from that of the previous prediction which involved only the refractive index contribution [3].

The properties of EIF are important to evaluate because they concern the design of any experiment in the field of atomic coherence. Not only will EIT experiments cause this form of cross focusing, but also experiments in inversionless lasing [4,5], where a strong coupling laser is used to prepare the atomic conditions, will experience similar effects, which cavity design will have to accommodate. Furthermore, access to ultrahigh refractive index without absorption [6,7] will give rise to lensing on the probe beams in a similar manner. Overall, the majority of the theories in these areas has, so far, dealt with plane-wave approximations, and the effects of spatial variations are now important to evaluate in light of several experiments being conducted worldwide.

### II. THEORY

In order to calculate the propagation of a probe beam within an EIF system, we proceed in two parts. The first part is to calculate the atomic conditions as they change radially

within the cell. This is accomplished by a standard density-matrix analysis for a three-level cascade atom, which includes the effect of Doppler broadening by numerical integration. The equations for the slowly varying density matrix components are [8,9]

$$\dot{\rho}_{11} = i\Omega_{12}(\tilde{\rho}_{21} - \tilde{\rho}_{12}) + \Gamma_{21}\rho_{22} + \Gamma_{31}\rho_{33}, \quad (1a)$$

$$\dot{\rho}_{22} = i\Omega_{12}(\tilde{\rho}_{12} - \tilde{\rho}_{21}) + i\Omega_{23}(\tilde{\rho}_{32} - \tilde{\rho}_{23}) - \Gamma_{21}\rho_{22} + \Gamma_{32}\rho_{33}, \quad (1b)$$

$$\dot{\rho}_{33} = i\Omega_{23}(\tilde{\rho}_{23} - \tilde{\rho}_{32}) - \Gamma_{32}\rho_{33} - \Gamma_{31}\rho_{33}, \quad (1c)$$

$$\dot{\tilde{\rho}}_{12} = -i(\Delta_1 - i\gamma_{12})\tilde{\rho}_{12} + i\Omega_{12}(\rho_{22} - \rho_{11}) - i\Omega_{23}\tilde{\rho}_{13}, \quad (1d)$$

$$\dot{\tilde{\rho}}_{23} = -i(\Delta_2 - i\gamma_{23})\tilde{\rho}_{23} + i\Omega_{23}(\rho_{33} - \rho_{22}) + i\Omega_{12}\tilde{\rho}_{13}, \quad (1e)$$

$$\dot{\tilde{\rho}}_{13} = -i(\Delta_1 + \Delta_2 - i\gamma_{13})\tilde{\rho}_{13} + i\Omega_{12}\tilde{\rho}_{23} - i\Omega_{23}\tilde{\rho}_{12}, \quad (1f)$$

with the subscripts referring to the three levels numbered from the lowest to the highest energy state. The detunings are defined as

$$\Delta_1 = \omega_1 - \omega_{12} - k_1 V_z, \quad (2a)$$

$$\Delta_2 = \omega_2 - \omega_{23} - k_2 V_z, \quad (2b)$$

with  $\omega_1$  and  $\omega_2$  denoting the frequencies of the applied optical fields,  $V_z$  the atomic velocity along the cell length,  $k_1$  and  $k_2$  the wave numbers of the applied optical fields, and  $\omega_{12}$  and  $\omega_{23}$  the energy separation of the appropriate levels. The Rabi frequencies are

$$\Omega_{12} = \frac{\mu_{12}E_1}{2\hbar}, \quad (3a)$$

$$\Omega_{23} = \frac{\mu_{23}E_2}{2\hbar}, \quad (3b)$$

with  $E_{1,2}$  the electric-field strength of the applied radiation and  $\mu_{12,23}$  the transition matrix elements for the transitions.

\*Present address: Sharp Laboratories of Europe Ltd., Edmund Halley Road, Oxford Science Park, Oxford OX4 4GA, England.

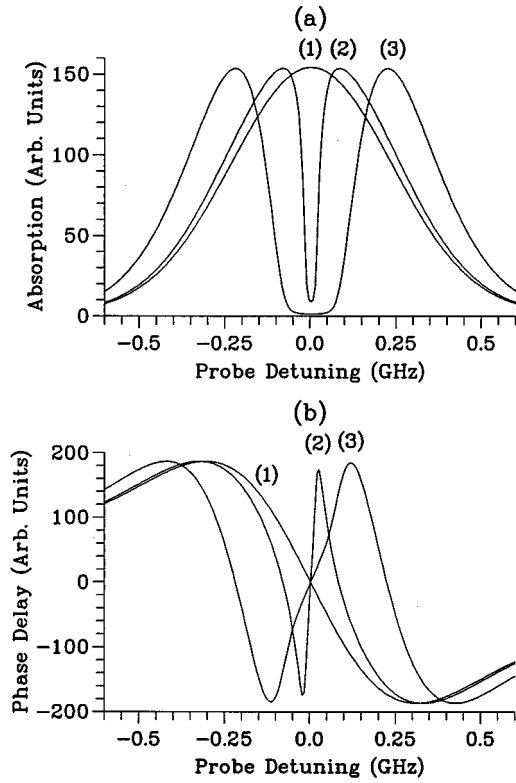


FIG. 1. The absorption (a) (from the imaginary part of the off-diagonal density matrix element  $\tilde{\rho}_{12}$ ) and the phase delay (b) (or refractive index change, from the real part of  $\tilde{\rho}_{12}$ ) against probe detuning ( $\Delta_2$ ) for coupling laser Rabi frequencies ( $\Omega_{23}$ ) of (1) 0 MHz, (2) 162 MHz, and (3) 440 MHz. The counterpropagating beams have 780 and 776 nm probe and coupling laser wavelengths, respectively; the gas temperature is 320 K; the coupling laser is assumed resonant ( $\Delta_2=0$ ).

The population decay rates ( $\Gamma_{ij}$ ) were set to  $\Gamma_{12}=40$  MHz,  $\Gamma_{23}=1.6$  MHz, and  $\Gamma_{31}=2.6$  MHz, and the coherence decay rates ( $\gamma_{ij}$ ) according to

$$\gamma_{12} = \frac{1}{2}\Gamma_{21}, \quad (4a)$$

$$\gamma_{23} = \frac{1}{2}(\Gamma_{21} + \Gamma_{31} + \Gamma_{32}), \quad (4b)$$

$$\gamma_{13} = \frac{1}{2}(\Gamma_{31} + \Gamma_{32}). \quad (4c)$$

The wavelengths and energy-level decay rates were chosen to reflect the experiments conducted with counterpropagating coupling and probe beams on the  $5S_{1/2}-5P_{3/2}-5D_{5/2}$  energy-level scheme in rubidium [10]. The equations are solved by invoking steady-state conditions (appropriate because of the employment of single-frequency continuous-wave lasers in the experiment) and thus setting all the time derivatives to zero. Equations (1a)–(1f) can then be split into nine real simultaneous equations, using the properties of the density matrix, and solved, using normal linear algebra routines.

Figure 1 displays three sets of results for (a) the absorption (from the imaginary part of  $\rho_{12}$ ) and (b) the phase delay (or change in refractive index, from the real part of  $\rho_{12}$ ) against the tuning of the probe laser. The three curves in each graph are taken for different radial points on the coupling laser profile. Curve (1) has a coupling laser Rabi frequency

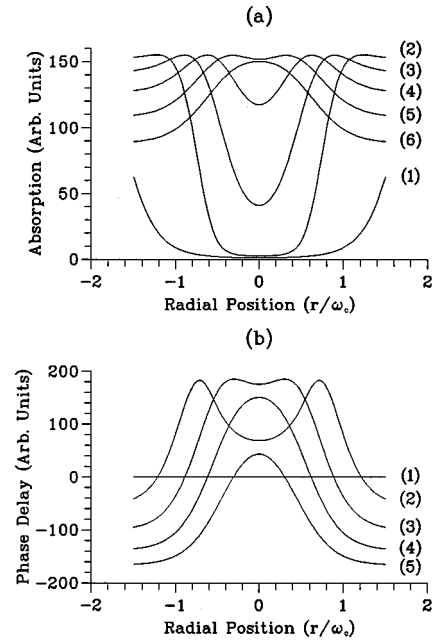


FIG. 2. The absorption (a) and phase delay (b) against radial position with respect to the center of the coupling laser Gaussian profile. Curves (1) to (5) in both plots and curve (6) in (a) correspond to probe detunings of 0, 0.05, 0.1, 0.15, 0.2, and 0.25 GHz, respectively. The radial position is scaled in units of the coupling laser waist size  $c$ . The peak coupling laser Rabi frequency is 440 MHz; other parameters are as in Fig. 1.

( $\Omega_{23}$ ) of zero and hence represents the conditions in the vapor outside of the coupling laser. Curve (2) is for the waist of the coupling laser with  $\Omega_{23}=162$  MHz, and curve (3) is for the center of the Gaussian profile with  $\Omega_{23}=440$  MHz. From these curves the radical changes in spatial conditions within the cell can be deduced. For example, with the probe tuning at line center, the middle of the probe beam will have low absorption, but the wings, if they extend outside the coupling laser profile, will have absorption. Conversely, at a probe detuning ( $\Delta_1$ ) of 0.25 GHz, the situation is actually reversed, with higher absorption on the axis.

To show the radial conditions clearly, Fig. 2 displays curves of (a) probe absorption and (b) phase delay calculated as the coupling laser Rabi frequency changes with a Gaussian distribution of waist size  $\omega_0$ . The individual curves correspond to different probe tunings relative to line center, as noted in the caption, but, in summary, curve (1) is for line center and the rest follow a progression in increasing detuning. Taking the absorption conditions first, we can see that there is a relatively wide transparency window for the probe to propagate through at line center, but this progressively narrows and becomes less pronounced as the probe tuning changes. We can expect this to clip the edges of a probe beam of similar width to the pump. As the detuning increases past the peak Rabi frequency of the coupling laser, the situation reverses, as noted above, and the absorption actually becomes greater on the axis, favoring the propagation of the outer edges of the probe beam. The refractive index also changes over this same detuning range. Initially, on zero detuning, the refractive index has no radial variation (as noted in [3]), but in curve (2) there is already a strong variation.

While  $-1 < r/\omega_0 < 1$ , the curvature displayed gives less phase delay on the axis and hence imposes a diverging curvature on the probe wave front. In later curves this is reversed and a converging curvature is imposed. However, the behavior of a probe beam in the cases described by curves (2) and (3) will be strongly dependent on the relative initial coupling and probe waist sizes due to the change in curvature with radial position. Therefore, distinct non-Gaussian probe output beams are to be expected.

In order to calculate the combined effects of these unusual radial variations in refractive index and absorption on the propagation of a probe beam through a cell prepared in this way by a coupling laser, a matrix solution of the Maxwell equation was followed as detailed by McDuff [11]. The treatment proceeds in only one transverse dimension, but it is valid for circularly symmetric conditions and is sufficient to give a good insight into the EIF phenomenon. The method proceeds by resolving the spatial information of the input beam and the medium's susceptibility to a linear combination of Hermite-Gaussian modes, using the properties of these to recast the wave equation into a matrix form amenable to numerical solution. Therefore the complex electric-field amplitude is expressed as

$$E(x, z) = \sum_{k=0}^{\infty} f_k(z) \psi_k(x), \quad (5)$$

where

$$\psi_k = C_k H_k \left( \frac{\sqrt{2}x}{r_0} \right) \exp \left[ - \left( \frac{x}{r_0} \right)^2 \right] \quad (6)$$

is the Gaussian-Hermite mode of order  $k$ . Furthermore,  $H_k$  is the Hermite polynomial of order  $k$ ;  $C_k$  is defined as

$$C_k = [\sqrt{\pi} r_0 2^{(i-1/2)} i!]^{1/2} \quad (7)$$

to ensure orthonormality of the modes; and  $r_0$  is a scaling constant. This constant is chosen to match the Gaussian-Hermite mode sizes to roughly the beam waist of the profile being decomposed to ensure swift convergence of the modes to form the beam profile. The propagation of the mode weights,  $f_k(z)$  is then given by

$$\frac{df_k}{dz} = -\underline{E} f_k, \quad (8)$$

and if the propagation matrix  $\underline{E}$  is independent of  $z$

$$f_k(z) = \exp(-\underline{E}z) f_k(z=0). \quad (9)$$

The propagation matrix  $\underline{E}$  takes into account spreading of the beam due to diffraction and the variation in absorption and refractive index experienced by the input beam. The definition is involved, and thus not worth repeating here, but is stated below Eq. (17) in Ref. [11].

In the implementation of this analysis it was assumed that the coupling laser beam is uniform throughout the cell. This assumption is realistic if the coupling beam is sufficiently collimated so as not to spread appreciably because of diffraction during propagation through the cell, and the probe beam is sufficiently weak so that the propagation of the coupling

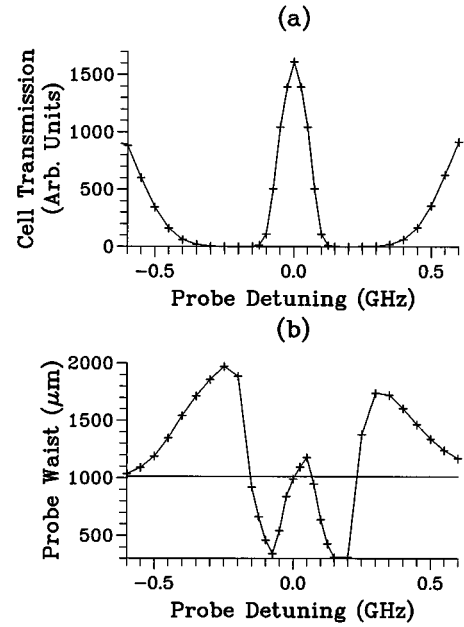


FIG. 3. The calculated transmitted probe irradiance (a) and waist size at the  $1/e$  point (b) for the probe electric-field amplitude after propagation through a 10 cm rubidium cell and 50 cm in air thereafter. The horizontal line in plot (b) is the undisturbed waist size for propagation over this distance. The initial probe beam waist size is 1 mm, the coupling laser waist size is 2 mm, and the peak Rabi frequency is 440 MHz; other parameters are as in Fig. 1.

beam is unaffected by the interaction medium. These assumptions could be removed by numerically integrating along the beam paths within the cell if necessary, but that complication is not required here to gain an understanding of the nature of electromagnetically induced focusing. In the implementation, the matrix exponential function was computed via a (4,4) diagonal Padé approximation [12] and decomposition up to the 40th order of Hermite-Gaussian modes was used (although this was extended up to the 60th mode if the coupling and probe beams were of widely different sizes, e.g., in Fig. 8). Since all the experimental observations of the beam size changes were made some distance back from the cell end, because of the counterpropagating arrangement the calculation was extended for propagation of a set distance through a homogeneous medium after the cell end. This was done by propagating each of the Hermite-Gaussian modes excited at the cell end for the chosen distance through air [13] and then recombining them with the appropriate weights,  $f_k(z)$  (as calculated above), at the observation plane.

The result for the beam waist at the  $1/e$  point after the probe beam has been propagated through a 10-cm vapor cell, and then 50 cm following that in air, is shown in Fig. 3, along with the corresponding intensity of the transmitted light. (This was calculated by numerical integration of the output beam profile.) The input beam waist sizes were 1 mm for the probe and 2 mm for the coupling laser. These relatively large beam sizes were chosen to avoid significant diffraction in these propagation distances and to allow the EIF behavior to be unambiguously observed. As can be seen, the behavior is predominantly one of defocusing in the highly

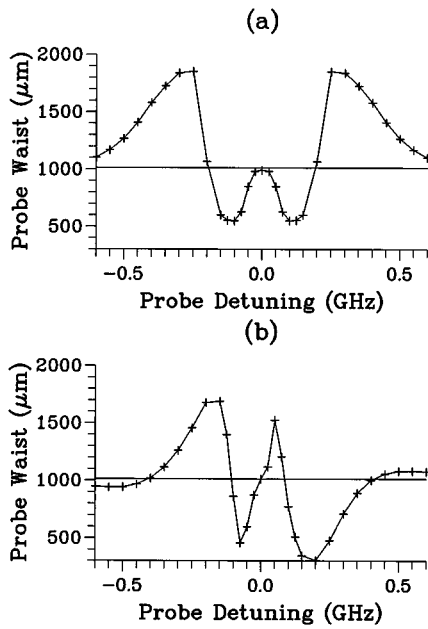


FIG. 4. The calculated probe waist size for the propagation conditions of Fig. 3 but ignoring the refractive index information (a) and the absorption information (b) within the vapor cell, leading to a separation of the effects of both contributions. The reference line and parameters are as in Fig. 3.

absorbing wings of the line and focusing within the EIT window. The overall behavior is rather different from that predicted by the simple method used in Ref. [3], and this is due to the effect of the spatially varying absorption conditions in the cell.

To illustrate the various contributions, the propagation was calculated via the model, ignoring first the refractive index information [Fig. 4(a)] and second, the absorption information [Fig. 4(b)] to separate the effects of the two contributions. The refractive-index-only calculation is very similar to the prediction of Ref. [3] and shows equal regions of focusing and defocusing around the zero detuning point. The absorption contribution is notably different, however, and is symmetric on either side of the zero detuning point. The focusing behavior near the central point is due to good EIT being experienced at the high-intensity regions of the coupling laser beam and poor EIT being experienced by the probe in the wings. This leads to clipping of the beam and a smaller transmitted spot. The defocusing in the wings is due to the opposite absorption variation. At a probe detuning similar to the peak coupling laser Rabi frequency induced in the atoms, the center of the probe beam experiences high absorption because the Autler-Townes component has been shifted to be on resonance with the probe. The edge of the probe beam, on the other hand, has less absorption because the Autler-Townes splitting is less and the probe detuning puts it in the wings of the absorption feature. These conditions can be seen in Figs. 1 and 2.

How these two contributions combine to give the resulting output depends on the propagation conditions after the cell. If the probe beam profile is interrogated at the end of the cell, it follows the absorption conditions very closely. The wave fronts have had a phase modulation impressed on them by the refractive index changes, but only after propagation

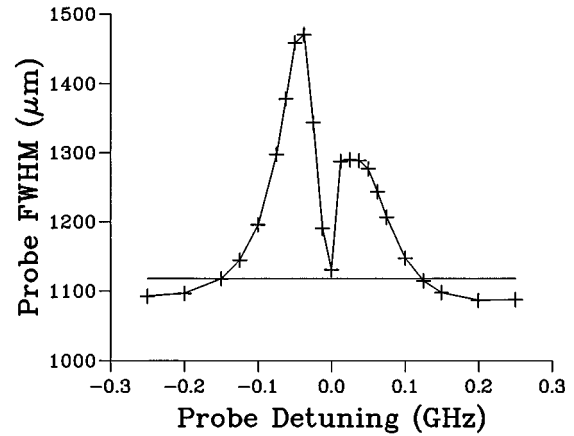


FIG. 5. The calculated probe FWHM after propagation through a 2 cm rubidium cell and 20 cm in air thereafter. The horizontal line denotes the waist size under diffraction-limited propagation conditions. The undistributed probe beam waist size is 55  $\mu\text{m}$ , with the focus located in the cell center. The coupling laser beam size is 110  $\mu\text{m}$ , and the peak Rabi frequency is 220 MHz; other parameters are as in Fig. 1.

over a distance will this translate into a focused or defocused beam. Thus the results of Fig. 3(b) consist of a mixture of the two contributions, as the refractive index contributions have led to an effect on roughly the same magnitude as the absorption contributions over the 50-cm propagation distance. Therefore, there will be different regimes for the observation of electromagnetically induced focusing: the near field, where the absorption effect will dominate; the far field, where the refractive index effect will dominate; and an intermediate regime, where both are important.

With this understanding in place, the parameters for the modeling were then chosen to reflect the experimental conditions more closely. The probe waist size was reduced to 55  $\mu\text{m}$ , with the focus taken at the cell center, and the coupling laser waist size was reduced to 110  $\mu\text{m}$ . With these relatively small waists, which give confocal parameters for the beams less than the overall propagation distance, diffraction effects will be important at the camera plane. In the experiments described in this paper, as opposed to those in Ref. [3], the cell length was 2 cm and the charge-coupled device (CCD) was placed approximately 20 cm after the cell end, so these parameters were used. The variation in probe full width at half maximum (FWHM) (as measured in the experiments) then predicted is shown in Fig. 5 and is very different to that of Fig. 3(b), where the probe does not experience a tight focus. Under these conditions, focusing within the cell from EIF will tighten the probe waist and lead to a larger spot size observed on the camera plane; similarly, defocusing will lead to the opposite effect. To display the different contributions from the absorption and refractive index variations, Fig. 6 repeats the calculations, ignoring the refractive index information (a) and then the absorption information (b). The results show that the overall variation is different from either of these and that the inclusion of the spatially varying absorption into the calculations is important.

It is interesting to see that there is a certain finite change in probe size at zero detuning and that this is entirely due to the absorption variation. In the earlier work [3], when ab-

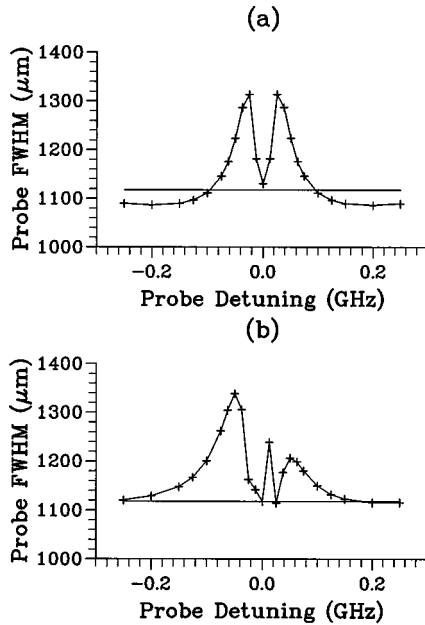


FIG. 6. The calculated probe FWHM for the propagation conditions of Fig. 5 but ignoring the refractive index information (a) and the absorption information (b) within the vapor cell. The reference line and parameters are as in Fig. 6.

sorption information was not taken into account, free-space propagation was predicted for the line center. With the appreciation of the radial change in absorption, this will now not be the case unless the probe is restricted to a small proportion of the coupling laser profile, where there is essentially no change in spatial conditions.

While there are many parameters in these calculations, one that is interesting to explore is the probe focal position. Figure 7 shows the predicted spot size variations for (a) the probe focused at the input to the cell and (b) the probe focused at the output end of the cell. They differ radically from the situation with the focus at the center of the cell (Fig. 5) and are almost mirror images of each other. Experimental confirmation of this change in conditions is given in the following section.

Finally we look briefly at the situation in which the probe waist size is initially greater than the coupling laser size, conditions opposite to those discussed above and in most EIT experiments because of the requirement for good transmission of the probe beam. This situation is interesting, as the probe laser effectively “sees” a soft-edged pinhole in the vapor at the line center, with low absorption on-axis and high absorption off-axis. Figure 8 shows a result for the probe beam profile at (a) the exit of the cell and (b) after 20 cm in air thereafter, with an initial probe size of  $500 \mu\text{m}$ , five times the coupling laser size. Distinct diffractionlike rings can be seen on the beam profile, mirroring those seen for propagation through a traditional pinhole. The radius of these will change as the transparency window changes size with probe detuning, experimental observation of these diffractionlike effects is given below.

### III. EXPERIMENTAL APPARATUS

The experiments conducted on the effects of electromagnetically induced focusing were carried out by using a 2-cm

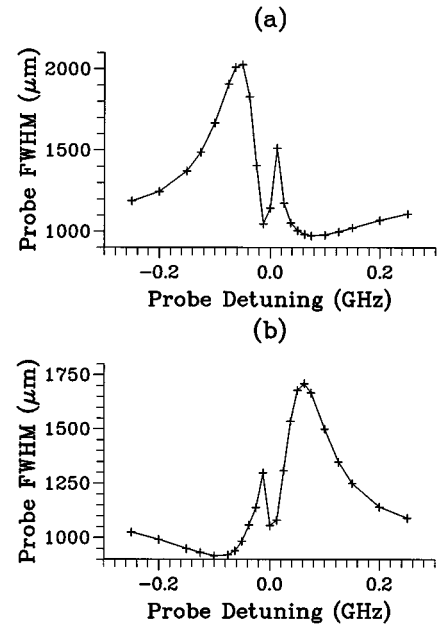


FIG. 7. The calculated probe FWHM for the propagation conditions of Fig. 5 but with the undisturbed probe focus located at the input window of the cell (a) and at the output window of the cell (b).

cell of rubidium vapor (Ophos Instruments). The cell was typically heated to around  $60^\circ\text{C}$  to give an appreciable amount ( $\geq 60\%$ ) of absorption of the focused probe beam. The laser radiation was supplied by two single-frequency cw Ti:sapphire lasers. The source of the probe field was a scanning Microlase MBR-110 laser tuned to the  $5S_{1/2}-5P_{3/2}$  transition at 780 nm, and the coupling field was supplied by a modified Schwartz Electro-Optic Titan cw laser tuned to the  $5P_{3/2}-5D_{5/2}$  transition at 776 nm. The laser beams were counterpropagated through the cell in order to reduce the two-photon Doppler width and so reduce the Rabi frequency at which EIT becomes apparent [14,15]. The probe laser power was attenuated to  $< 300 \mu\text{W}$  in order to minimize the effect of self-focusing, which could distort the results. After traveling through the cell, a portion of the probe beam was sampled by a pellicle beam splitter and directed onto a CCD array at a distance of 20 cm from the cell end. The total intensity of the incident light was found by integration of the pixel values, and the FWHM of the probe beam was measured to show the effects of EIF. A schematic of the experimental setup is shown in Fig. 9.

The coupling laser provided up to 500 mW of power and was focused into the cell by a 40-cm lens to give a waist size of  $150 \mu\text{m}$ . The confocal parameter was therefore almost nine times the cell length, giving a roughly constant axial intensity. The probe beam was focused to a  $55 \mu\text{m}$  waist, giving a confocal parameter of 2.4 cm, roughly similar to the cell length.

### IV. EXPERIMENTAL RESULTS

The variation in probe waist size due to EIF was found to be a good fit to the theoretical model in the two boundary conditions of focusing the probe beam at the front [Fig.

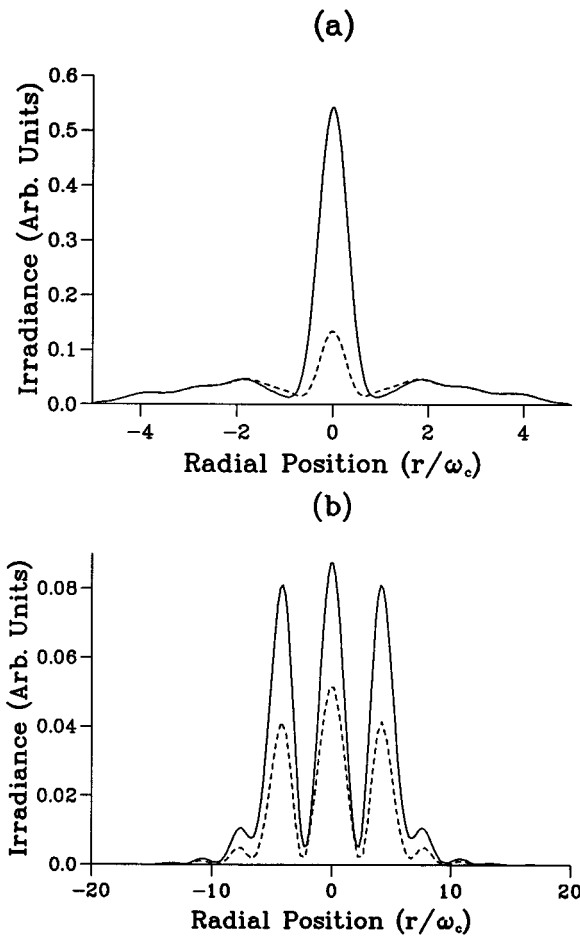


FIG. 8. The calculated probe radial intensity profile at the end of the 2-cm cell (a) and after a further 20-cm propagation in air (b). The solid line is for a probe detuning of 100 MHz, and the dashed line for a probe detuning of 150 MHz. The radial position is scaled in units of the coupling laser waist size  $c$ . The input probe laser waist size is  $500\ \mu\text{m}$ , the coupling laser beam size is  $100\ \mu\text{m}$ , and the peak Rabi frequency is 440 MHz; other parameters are as in Fig. 1.

10(a)] and back [Fig. 10(b)] of the cell. In Fig. 10(a) the beam experiences a wide frequency region of defocusing before the EIT peak and then quickly focuses, defocuses, and then refocuses over the EIT region itself. In Fig. 10(b) the opposite occurs, with the wide defocused region now cen-

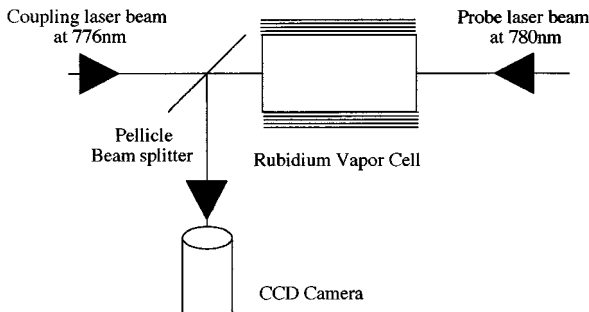


FIG. 9. A schematic of the experimental setup, showing the arrangement of the laser beams, vapor cell, and CCD camera.

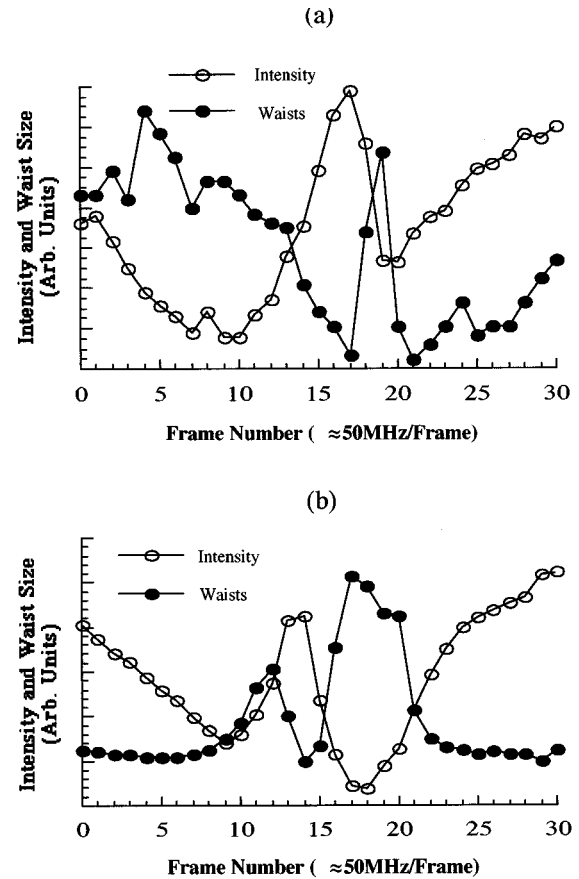


FIG. 10. The experimental variation of probe FWHM and intensity when the probe is focused (a) at the input window of the cell and (b) at the output window of the cell. The probe is focused on the  $55\text{-}\mu\text{m}$  waist; the coupling laser is focused on the  $150\text{-}\mu\text{m}$  waist.

tered over the absorption after the EIT peak. These behaviors should be compared to the corresponding theoretical predictions displayed in Fig. 7.

The behavior of the probe beam when focused in the center of the cell was found to vary between different experimental traces. In general the experimentally measured beam waists, as shown in Fig. 11, followed the behavior predicted by theory, with two defocusing regions both within the EIT peak. The strong focusing at the transmission peak was always observed; this is a very abrupt feature, which typically occurs over a probe tuning range of 25–50 MHz at these coupling laser powers. The relative height of the two peaks was found to vary between traces, and the peak edges were sometimes blurred by defocusing at the transparency edges. This is perhaps not surprising, as a 1-cm change in the focal position in either direction leads to a radical change in the conditions within the cell. Furthermore, changes in temperature and beam overlap are also capable of causing radical changes in the probe behavior observed.

The generally good fit to the theoretical treatment outlined in the preceding section for the three different focal positions within the cell shows that both the refractive and absorptive contributions must be used to correctly predict the EIF behavior. Ignoring either of these contributions leads to far different behavior, which cannot be matched to the experimental results taken in what is effectively the intermediate region

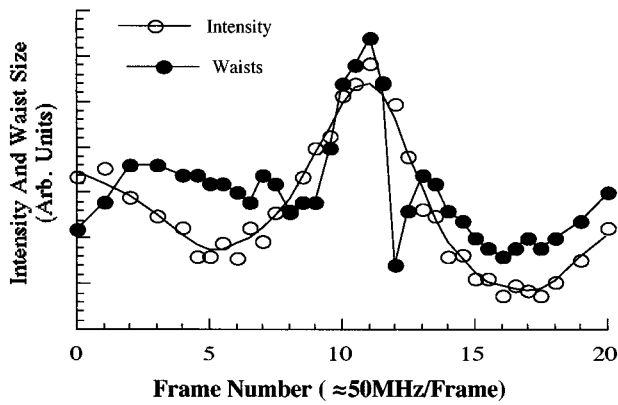


FIG. 11. The experimental variation of probe FWHM and intensity when the probe is focused in the center of the cell. The probe is focused to  $55\ \mu\text{m}$  waist; the coupling laser is focused on the  $150\text{-}\mu\text{m}$  waist.

between absorptive and refractive domination.

A novel effect of EIF is seen dramatically when the probe beam waist size is much larger than the coupling laser waist. In this experiment the probe beam was left unfocused and had a waist size of approximately  $2\ \text{mm}$ . Figure 12 shows the probe beam after propagation through the cell at a tuning close to the transparency peak. Clear diffractionlike rings can now be seen on the probe laser intensity profile. These rings can be seen to contract as the probe is scanned through resonance. The change in the ring structure is shown in Fig. 13 for different probe frequency detunings within the EIT region. This behavior follows the circular symmetry of the coupling laser beam intensity profile and can be changed by inserting a cylindrical lens into the pump beam, hence producing a slitlike focus in the cell. As expected, the probe now diffracts into a series of linear fringes once it has been transmitted through the transparency slit, as shown in Fig. 14.

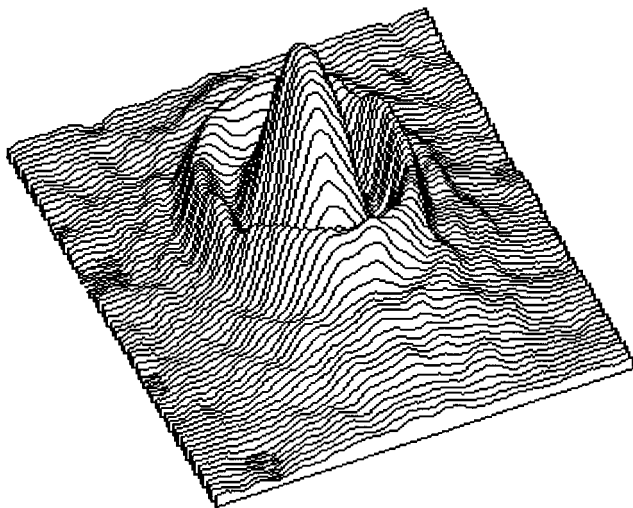


FIG. 12. A three-dimensional plot of the probe beam as it appears on the CCD camera after being transmitted through a much smaller circular transparency. The probe beam has a  $2\text{-mm}$  waist; the coupling laser has a  $150\text{-}\mu\text{m}$  waist.

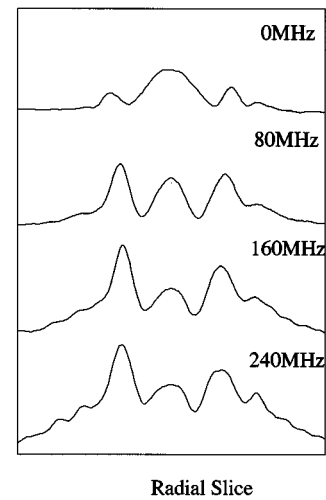


FIG. 13. The variation with frequency of the ring pattern observed in Fig. 12.

## V. CONCLUSIONS

In summary, we have shown the importance of the spatially varying absorption conditions during EIT in altering the probe beam propagation conditions. Regions of focusing and defocusing are caused by these conditions and combine with the spatially varying refractive index conditions to lead to a complex overall variation in the probe beam spot size. Results were presented for the expected spot size variations as the probe laser tunes under various parameters, showing the importance of the relative beam sizes in changing the output characteristics. Also, under moderate focusing conditions, the position of probe beam focus within the cell was shown to be important in determining the observed variation in probe laser beam size after the cell, both theoretically and experimentally. Furthermore, the theory correctly predicted the emergence of diffractionlike rings on the probe spot

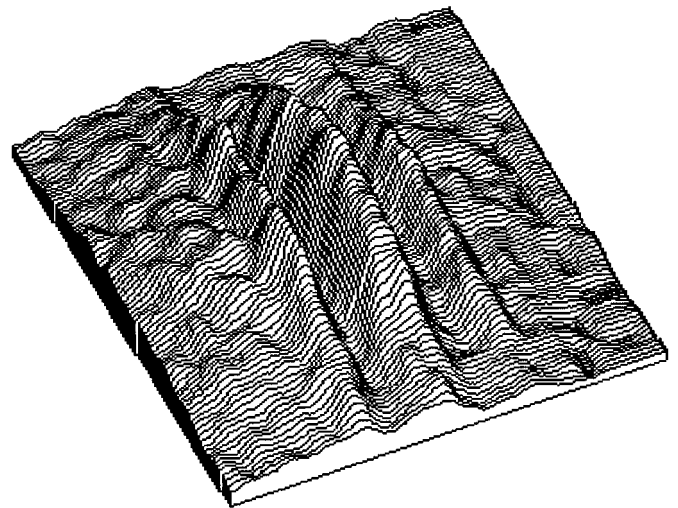


FIG. 14. A three-dimensional plot of the probe beam as it appears on the CCD camera after being transmitted through a slitlike transparency imposed on the vapor by a cylindrical lens. The probe beam has a  $2\text{-mm}$  waist.

when a large probe laser beam is used to illuminate an EIT region created by a smaller coupling laser beam. Experiments were carried out in this regime, in which the coupling laser imprints a transparency aperture in the medium, using either a circular or a cylindrical lens. The probe was seen to treat this light-induced aperture in much the same way as it would a solid aperture, with ring and slit diffractionlike pat-

terns evident in the probe beam profile at the camera surface.

These results show the importance of taking the spatially varying conditions of an experiment into account when designing experiments in the EIT, inversionless lasing, and phaseonium areas of study. For example, cavity design for inversionless lasers will be affected by considerations of EIF and beam shaping by absorption.

- 
- [1] K. J. Boller, A. Imamolu, and S. E. Harris, *Phys. Rev. Lett.* **66**, 2593 (1991).
- [2] M. Xaio *et al.*, *Phys. Rev. Lett.* **74**, 666 (1995).
- [3] R. R. Moseley *et al.*, *Phys. Rev. Lett.* **74**, 670 (1995).
- [4] O. Kocharovskaya, *Phys. Rep.* **219**, 175 (1992).
- [5] P. Mandel, *Contemp. Phys.* **34**, 235 (1993).
- [6] M. Fleischhauer *et al.*, *Phys. Rev. A* **46**, 1468 (1992).
- [7] M. O. Scully, *Phys. Rep.* **219**, 191 (1992).
- [8] R. R. Moseley *et al.*, *Phys. Rev. A* **50**, 4339 (1994).
- [9] R. R. Moseley, Ph.D. thesis, University of St. Andrews, 1994 (unpublished).
- [10] R. R. Moseley *et al.*, *Opt. Commun.* **119**, 61 (1995).
- [11] R. McDuff, *Appl. Opt.* **29**, 802 (1990).
- [12] Y. Y. Lin and L. P. Hwang, *Comput. Chem.* **16**, 285 (1992).
- [13] A. Yariv, *Optical Electronics*, 4th ed. (Saunders, Philadelphia, 1991).
- [14] J. Gea-Banacloche *et al.*, *Phys. Rev. A* **51**, 576 (1995).
- [15] D. J. Fulton *et al.*, *Phys. Rev. A* **52**, 2302 (1995).